

Improving the Smoothed Particle Hydrodynamics with an integral approach to calculate gradients

Domingo García-Senz¹, Rubén M. Cabezón², and José Antonio Escartín¹

¹ Dept. de Física i Enginyeria Nuclear, Universitat Politècnica de Catalunya. Compte d'Urgell 187, 08036 Barcelona (Spain) and Institut d'Estudis Espacials de Catalunya. Gran Capità 2-4, 08034 Barcelona, Spain

² Departament Physik, Universität Basel. Klingelbergstrasse 82, 4056 Basel, Switzerland and Dept. de Física i Enginyeria Nuclear, Universitat Politècnica de Catalunya. Compte d'Urgell 187, 08036, Barcelona, Spain

ABSTRACT

Context. The smoothed particle hydrodynamics (SPH) technique is a well known numerical method which has been applied to simulate the evolution of a large variety of systems. Modern astrophysical applications of the method rely in the Lagrangian formulation of fluid Euler equations which is fully conservative. A different scheme, based on a matrix approach to the SPH equations is currently being used in computational fluid dynamics (CFD). These matrix formulations achieve better interpolations of the physical magnitudes but they are, in general, not fully conservative. The matrix approach to the Euler equations has never been used in astrophysics. **Aims.** Develop and check a fully conservative SPH scheme based on a tensor formulation which can be applied to simulate astrophysical systems.

Methods. In the proposed scheme derivatives are calculated from an integral expression which leads to a tensor, rather than vectorial, estimation of gradients and reduces to the standard formulation in the continuum limit. The new formulation improves the interpolation of physical magnitudes, leading to a set of conservative equations which looks similar to those of standard SPH. The resulting scheme was checked using a variety of well known tests, all of them simulated in two dimensions. An application of the proposed tensor method to astrophysics was also discussed by simulating the stability of a sun-like polytrope calculated in three dimensions.

Results. The proposed scheme was able to improve the results of standard SPH in the two dimensional tests, especially in the simulation of subsonic hydrodynamic instabilities. The results concerning the stability of the sun-like polytrope suggest that the new method can be used in astrophysics to carry out three dimensional calculations with a computational cost only slightly higher (i.e. $\leq 50\%$ for a serial code) than that of standard SPH formulation.

Conclusions. A formalism based on a matrix approach to Euler SPH equations was developed and checked. The new scheme is more accurate due to the re-normalization imposed to the interpolations, fully conservative and probably less prone to undergo the tensile instability. The analysis of several test cases suggest that the method may improve the simulation of both, subsonic and supersonic systems. An application of the tensor method to astrophysics was, for first time, successfully carried out. These encouraging results indicates that more work should be invested in the applications of matrix SPH formulations to astrophysics.

Key words. Numerical hydrodynamics, smoothed particle hydrodynamics

1. Introduction

The hydrodynamic method known as smoothed particle hydrodynamics (SPH) is a grid less lagrangian approach to continuum mechanics devised by Gingold & Monaghan (1977) and Lucy (1977). As demonstrated in an endless amount of applications in computational fluid dynamics, ranging from large scale astrophysical simulations to nuclear physics at fermi level, SPH is a robust and confident way to simulate the dynamical evolution of deformed systems. The success of SPH strongly relies in the way how gradients are estimated. For example, the value of density in a given spatial coordinate is obtained from particles located in the neighborhood using an interpolating function called *kernel*. As the kernel is an analytical differentiable function, it is easy to obtain gradients just taking the gradient of this weighting kernel function. In that way it is not difficult to write the Euler equations of fluid mechanics in terms of the kernel and its derivatives (Monaghan 1992, 2005).

Despite the success, SPH has also a number of shortcomings and weak points which make the technique less useful than it should be to handle a number of well identified problems. First

of all, the numerical noise is usually larger than in other techniques, which pose a problem for applications involving very subsonic movements, as it is the case of the hydrodynamical instabilities. Another difficulty has to do with the use of the artificial viscosity (AV) formalism to handle shock waves and also to smooth the inherent presence of noise. Several solutions and recipes have been invoked to handle with these problems, none of them totally satisfactory, among them: variable AV coefficients (Morris 1997), artificial heat fluxes to smooth pressure discontinuities (Price 2008), non standard approximations to the momentum equation (Abel 2011) and a refined treatment of kernel interpolations as in the technique known as Moving Least Squares interpolation (i.e. *MLS*; Dilts 1999).

In this paper we present an approach to the momentum and energy equations which combines a novel way to estimate gradients and the variational principle, and allows for an improved modeling of physical phenomena, especially in those systems subjected to small perturbations. The proposed formalism, based on an integral approach to the derivatives (*IAD*), includes the standard formulation as a particular case. It leads to a matrix

formulation similar to that of MLS methods but the form of the SPH equations in IAD remains closer to that of standard SPH. The text is organized as follows. In Sect. 2 the mathematical formalism to calculate gradients is described and discussed. In Sect. 3 a formulation of the momentum equation compatible with the variational Euler-Lagrange principle in the SPH framework is developed. A consistent and fully conservative energy equation is proposed in the same section. Section 4 is devoted to validate the hydrocode through the simulation of four known tests where standard SPH has, in more or less degree, difficulties to handle with. In Sect. 5 we elaborate an extension of the method which, combining exact estimation of the derivative of linear functions and good momentum and energy conservation, can be applied to simulate linearised systems. The ability of the proposed method to simulate the structure of real 3D astronomical bodies is discussed in Sect. 6. Finally, the main conclusions of our work, as well as some comments about the shortcomings of the developed scheme and future lines of improvement are outlined in the last chapter, devoted to conclusions.

2. Integral approach to first derivatives

There is an ample literature relative to the treatment of first and second derivatives in SPH (Monaghan 2005; Rosswog 2009). In the following we take a different route to estimate first derivatives which leads to a more general expression than the most common extant derivative procedures. Our method keeps some resemblance to those known as *MLS* methods where interpolations relative to gradient estimation were constrained to enhance linearity by imposing a minimization procedure to the errors.

Inspired by the treatment of second derivatives (Brookshaw 1985) we define an integral expression from which we will make the estimation of gradients. As in the case of second derivatives, it is expected that an integral approach will lead to a less noisy estimation of first derivatives. Therefore, the following integral is defined:

$$I(\mathbf{r}) = \int_V [f(\mathbf{r}') - f(\mathbf{r})] (\mathbf{r}' - \mathbf{r}) W(|\mathbf{r}' - \mathbf{r}|, h) dr'^3, \quad (1)$$

where $f(r)$ is any differentiable function and $W(|\mathbf{r}' - \mathbf{r}|, h)$ is a spherically symmetric interpolating kernel, usually a sharp-like Gaussian of width h (h is usually referred as the smoothing length). The size of h is often interpreted as the local resolution of the simulation. Expanding the factor $[f(\mathbf{r}') - f(\mathbf{r})]$ until first order:

$$f(\mathbf{r}') - f(\mathbf{r}) = \nabla \mathbf{f} \cdot (\mathbf{r}' - \mathbf{r}) + \text{higher order terms}, \quad (2)$$

and writing,

$$(\mathbf{r}' - \mathbf{r}) = (x'_1 - x_1)\mathbf{i} + (x'_2 - x_2)\mathbf{j} + (x'_3 - x_3)\mathbf{k}. \quad (3)$$

Equation (1) can be expressed as a matrix equation:

$$\begin{bmatrix} \partial f / \partial x_1 \\ \partial f / \partial x_2 \\ \partial f / \partial x_3 \end{bmatrix} = \begin{bmatrix} \tau_{11} & \tau_{12} & \tau_{13} \\ \tau_{21} & \tau_{22} & \tau_{23} \\ \tau_{31} & \tau_{32} & \tau_{33} \end{bmatrix}^{-1} \begin{bmatrix} I_1 \\ I_2 \\ I_3 \end{bmatrix}, \quad (4)$$

where

$$\tau_{ij} = \int (x'_i - x_i)(x'_j - x_j) W(|\mathbf{r}' - \mathbf{r}|, h) dr'^3; i, j = 1, 3 \quad (5)$$

and

$$I_k = \int [f(\mathbf{r}') - f(\mathbf{r})] (x'_k - x_k) W(|\mathbf{r}' - \mathbf{r}|, h) dr'^3; k = 1, 3. \quad (6)$$

Once the linear system (4) is solved we get the value of the gradient of the function f . In the case of spherically symmetric kernels: $\tau_{11} = \tau_{22} = \tau_{33}$ and $\tau_{ij} = \tau_{ji} = 0, i \neq j$. Taking for instance the Gaussian kernel:

$$W^G(u, h) = \frac{1}{\pi^{n/2}} \exp(-u^2), \quad (7)$$

where n is the dimensionality of space and $u = \frac{(|\mathbf{r}' - \mathbf{r}|)}{h}$, it leads to $\tau_{ii} = \frac{h^2}{2}$. Therefore, for the Gaussian kernel the gradient of f reduces to:

$$\nabla \mathbf{f} = \int [f(\mathbf{r}') - f(\mathbf{r})] \nabla W(|\mathbf{r}' - \mathbf{r}|, h) dr'^3, \quad (8)$$

which is the same expression as Eq. (2.13) in Monaghan (2005) although obtained through a different procedure. Because of standard kernels are spherically symmetric the expression (8) can be further simplified to:

$$\nabla \mathbf{f} = \int f(\mathbf{r}') \nabla W(|\mathbf{r}' - \mathbf{r}|, h) dr'^3, \quad (9)$$

which in SPH parlance becomes:

$$\nabla_a \mathbf{f} = \sum_b \frac{m_b}{\rho_b} f_b \nabla W_{ab}(h_a), \quad (10)$$

which because of its simplicity and good performance has become the most popular procedure to make first derivatives in SPH. Therefore Eq. (10) appears as a *particular case* of IAD , Eq. (4).

Nevertheless many of the above symmetry properties of tensor $\mathcal{T} \equiv \{\tau_{ij}\}$ are lost when integrals are converted into finite summations. For example, the elements on the diagonal of matrix \mathcal{T} in Eq. (4) do not necessarily have the same value and elements out the diagonal can be different to zero. However the formulation of the first derivative in terms of the matrix Eq. (4) has a very interesting feature: the derivative of a linear function is always exact by construction. The demonstration of such property is straightforward in 1D SPH:

$$\left(\frac{df}{dx} \right)_a = \frac{\sum_b \frac{m_b}{\rho_b} (f_b - f_a) (x_b - x_a) W_{ab}}{\sum_b \frac{m_b}{\rho_b} (x_b - x_a)^2 W_{ab}}, \quad (11)$$

taking $f_a = px_a + q, f_b = px_b + q$ the expression above gives $\left(\frac{df}{dx} \right)_a = p$.

In *two dimensions* the explicit solution for Eq. (4) is written as:

$$\frac{\partial f}{\partial x_1} = c_{11} I_1 + c_{12} I_2; \quad \frac{\partial f}{\partial x_2} = c_{21} I_1 + c_{22} I_2, \quad (12)$$

where:

$$\begin{aligned} c_{11} &= \left(\tau_{11} - \frac{\tau_{12}^2}{\tau_{22}} \right)^{-1}; & c_{12} &= - \left(\frac{\tau_{12}}{\tau_{22}} \right) \left(\tau_{11} - \frac{\tau_{12}^2}{\tau_{22}} \right)^{-1}; \\ c_{21} &= - \left(\frac{\tau_{12}}{\tau_{11}} \right) \left(\tau_{22} - \frac{\tau_{12}^2}{\tau_{11}} \right)^{-1}; & c_{22} &= \left(\tau_{22} - \frac{\tau_{12}^2}{\tau_{11}} \right)^{-1}. \end{aligned} \quad (13)$$

Unfortunately direct application of the tensor scheme above leads to SPH equations of movement which are not fully conservative. Nevertheless a slight modification of the scheme makes it possible to build exact conservative equations. To do that we take advantage of the symmetry properties of the kernel to approach the vector $\mathbf{I}(\mathbf{r})$ as:

$$I(\mathbf{r}) = \int [f(\mathbf{r}') - f(\mathbf{r})] (\mathbf{r}' - \mathbf{r}) W(|\mathbf{r}' - \mathbf{r}|, h) d\mathbf{r}'^3 \simeq \sum_b \frac{m_b}{\rho_b} f(\mathbf{r}_b) (\mathbf{r}_b - \mathbf{r}_a) W(|\mathbf{r}_b - \mathbf{r}_a|, h_a). \quad (14)$$

From this on the formulation which comes out after putting Eq. (14) into Eq. (4) will be labeled as IAD_0 . This restricted interpretation of Eq. (4) sacrifices exact derivative of linear functions in order to preserve exact conservation of momentum and energy. Still, we present below strong indications that using IAD_0 leads to a better approach to the derivative of linear functions than the standard procedure given by Eq. (10), especially when a small or moderate number of neighbors is used to compute summations. This point can be illustrated by the following numerical experiments.

As a first test we simulate a static system where we compare the gradient of a linear distribution of density in one dimension obtained with IAD , IAD_0 and standard schemes as a function of the number of neighbors n_b . A linear density profile $\rho(x) = 1 + x$ was obtained putting $N=100$ equidistant particles with the adequate mass along the x -axis. The density was calculated using:

$$\rho_a = \sum_b m_b W_{ab}(|\mathbf{r}_b - \mathbf{r}_a|, h_a). \quad (15)$$

Note that even though IAD should give exact derivative in practice it never does owing to the small errors in the calculation of density. It is also worth noting that the standard calculation of the derivative has two additional potential sources of error. For a linear density profile $\rho_b = \rho_a + p(x_b - x_a)$ and using Eq.(10) we have:

$$\left(\frac{d\rho}{dx}\right)_a^{STD} = \sum_b \frac{m_b}{\rho_b} \rho_a \nabla_a W_{ab} + p \sum_b \frac{m_b}{\rho_b} (x_b - x_a) \nabla_a W_{ab} \quad (16) \\ = \epsilon_1 + \epsilon_2 p,$$

where p is the 'exact' derivative and $\epsilon_1 \simeq 0$, $\epsilon_2 \simeq 1$. On the other hand there is only one source of error, $\epsilon_3 \simeq 0$, if IAD_0 is used:

$$\left(\frac{d\rho}{dx}\right)_a^{IAD_0} = \frac{\sum_b \frac{m_b}{\rho_b} \rho_a (x_b - x_a) W_{ab}}{\sum_b \frac{m_b}{\rho_b} (x_b - x_a)^2 W_{ab}} + p = \epsilon_3 + p, \quad (17)$$

In Fig. 1 (upper and bottom left) there is represented the value of the relative error of the derivative $\epsilon = |\frac{d\rho}{dx} - p|/p$, with respect to the analytical value p as a function of the smoothing length h , normalized to the inter-particle distance Δ , for the Gaussian and cubic spline kernels respectively. With independence on the kernel the error when full IAD linear interpolation was used is always much lower than for the other methods. When IAD_0 or standard derivative were used the error appreciably rose. The error is high once the smoothing length becomes lesser than the inter-particle distance but it rapidly decays as h rises, as expected. Nevertheless the error in the standard calculation always remained larger, especially for a low or moderate

number of neighbors, $n_b \leq 5$ no matter the kernel we used but especially for the cubic spline. Because the particle sample is highly ordered the error curve of the Gaussian kernel is much smoother than that of the cubic spline owing to the infinite range of the kernel. It was checked that when the Gaussian is truncated to $2h$ the error profile becomes qualitatively similar to that of the cubic spline. On the other hand the error profile for IAD_0 follows almost exactly the error curve for the gradient of density calculated as a simple quotient $\frac{\rho_b - \rho_a}{x_b - x_a}$ for adjacent particles. In this sense IAD_0 seems to be more coherent with the computed density distribution of the sample than IAD , a trend which also holds in 2D, as shown below.

The contributions to the total error of ϵ_1 , ϵ_2 and ϵ_3 in expressions (16) and (17) are shown in the rightmost part of Fig. 1. The contribution of ϵ_1 and ϵ_3 are similar but the error ϵ_2 , which affects only to the standard scheme and exhibits a large oscillation in the case of compact supported interpolators, represents the main channel to the total error of the derivative. Usually the higher the dimensionality is, the better tensor methods are. Thus we have conducted a similar numerical experiment in more than one dimension where the matrix approach can potentially be more beneficial.

As a second test, a bi-dimensional system was set using a sample of $N=62\,500$ equally spaced particles on a two-dimensional lattice. The mass of the particles along the x -axis was conveniently modified to reproduce a linear, $\rho(x, y) = 1 + x$ density profile. The first derivative of the density, $\frac{\partial \rho}{\partial x}$ for different number of neighbors was obtained using Eqs. (4) and (10). In the upper row of Fig. 2 it is shown the relative error of the derivative, $\epsilon = |\frac{\partial \rho}{\partial x} - p|/p$, with respect to the analytical value p as a function of the smoothing length. Calculations were carried out using the Gaussian and the cubic spline kernels. The trend here is similar to that of the 1D calculation but magnitudes fluctuate less, especially in the case of the cubic spline. When the number of neighbors is large the error is small in all three methods but tensor schemes are more accurate than the standard procedure. Nevertheless, below $h \leq 1.5\Delta$ the error curve steepens and for $h < \Delta$ standard SPH begins to give unacceptable results while the tensor estimations to the derivative still work. This result is also in agreement to the 1D calculation shown in Fig. 1 which shows that working with $n_b \leq 3, 4$ in 1D dimension may give an appreciable error in the derivative of a linear function if Eq. (10) is used to compute derivatives. As in the one dimensional case the gradient calculated as a direct fraction $\frac{\rho_b - \rho_a}{x_b - x_a}$ (crosses in Fig. 2) remained closer to the results obtained using IAD_0 .

Finally, we have considered a spherically symmetric linear profile $\rho(x, y) = 1 + r$ being $r = \sqrt{x^2 + y^2}$. In the bottom row of Fig. 2 there is shown the value of the relative error ϵ as a function of $h(\Delta)$. The profile of the error follows a slightly different trend than in the previous case. As before, the error is high when the smoothing length is lesser than the inter-particle distance but in the case of the Gaussian kernel there is a minimum in the error profile at $h \simeq 1.1\Delta$. From that point on the error smoothly increases. Such behavior is not so accentuated in the case of the cubic spline where the error curve roughly stabilizes above $h = 2\Delta$. Therefore there is an optimal value of h which minimize the errors in the first derivative in this case. Close to the centre linearity is lost because of the symmetry imposed to the distribution. When the value of h is large interpolations are affected by that geometrical constraint and, at some point, the advantages of working using a large smoothing length are lost. Nevertheless, the error profile calculated using IAD_0 is always lesser than that of the standard scheme. Again the gradient of

density estimated as a simply quotient $\frac{\rho_b - \rho_a}{r_b - r_a}$ is better reproduced by IAD_0 than for the other schemes.

3. The momentum and energy SPH equations using IAD_0

Nowadays the most accurate formulation of momentum equation in SPH comes from the variational principle. It has been shown (Monaghan 2005, and references therein) how the solution of the Euler-Lagrange equations leads naturally to a very symmetric scheme which includes the effects of spatial gradients of the smoothing length. The resulting equation conserves momentum by construction and, equally important, it leads to an exact energy conservation for non dissipative systems. It is shown below how the tensor approach built using the IAD_0 scheme can also be made compatible to the variational principle.

The Lagrangian of the system is evaluated as:

$$L = \sum_b m_b \left(\frac{1}{2} v_b^2 - u_b(\rho_b, s_b) \right), \quad (18)$$

where v_b , u_b and s_b are the velocity, specific internal energy and specific entropy of particle b . With that Lagrangian and assuming isentropic evolution the Euler-Lagrange equations subjected to the constraint $\rho h^3 = \text{constant}$, lead to the following equation of movement (Springle & Hernquist 2002)¹:

$$m_a \ddot{x}_a = - \sum_b m_b \frac{P_b}{\rho_b^2 \Omega_b} \nabla_a \rho_b, \quad (19)$$

where $\Omega_b = (1 - \partial\rho/\partial h \sum_c m_c \partial W_{bc}/\partial h)$ is a term accounting for the gradient of h . The i -component in Eq. (19) can be written:

$$m_a \ddot{x}_{i,a} = - \sum_{b \neq a} m_b \frac{P_b}{\rho_b^2 \Omega_b} \frac{\partial \rho_b}{\partial x_{i,a}} - m_a \frac{P_a}{\rho_a^2 \Omega_a} \frac{\partial \rho_a}{\partial x_{i,a}}. \quad (20)$$

An estimation of the density gradients using the tensor Eq. (4) is:

$$\nabla \rho = \mathbf{C} \mathbf{I}, \quad (21)$$

where $\mathbf{C} = \mathcal{T}^{-1}$. Elements of matrix \mathcal{T} are those defined in Eq. (5) after changing integrals to summations. For particle a they read:

$$\tau_{i,j,a} = \sum_b \frac{m_b}{\rho_b} (x_{i,b} - x_{i,a})(x_{j,b} - x_{j,a}) W_{ab}(h_a), \quad (22)$$

and the j -component of vector \mathbf{I} in the IAD_0 approach is:

$$I_{j,a} = \sum_b m_b (x_{j,b} - x_{j,a}) W_{ab}(h_a). \quad (23)$$

Thus, for particle a the i -component of density gradient is:

$$\begin{aligned} \frac{\partial \rho_a}{\partial x_{i,a}} &= \sum_{j=1}^d c_{ij,a}(h_a) I_{j,a}(h_a) = \\ & \sum_{j=1}^d \sum_b m_b c_{ij,a}(h_a) (x_{j,b} - x_{j,a}) W_{ab}(h_a), \end{aligned} \quad (24)$$

¹ In that paper the ∇h contribution is estimated using the Lagrange multipliers technique.

where $c_{ij,a}$ are the elements of matrix \mathbf{C} associated to particle a , and d is the dimension of the space. Explicit expressions for these elements in Cartesian 2D were given by Eq. (13). Equation (24) can be used to directly compute the second term on the right of Eq. (20).

Similarly for particle b :

$$\frac{\partial \rho_b}{\partial x_{i,b}} = \sum_{j=1}^d \sum_c m_c c_{ij,b}(h_b) (x_{j,c} - x_{j,b}) W_{bc}(h_b). \quad (25)$$

To calculate $\frac{\partial \rho_b}{\partial x_{i,a}}$ we use Eq. (15):

$$\frac{\partial \rho_b}{\partial x_{i,a}} = -m_a \frac{\partial W_{ab}(h_b)}{\partial x_{i,b}}. \quad (26)$$

The last term in Eq. (26) also appears during the evaluation of $\nabla_b \rho_b$:

$$\frac{\partial \rho_b}{\partial x_{i,b}} = \sum_c m_c \frac{\partial W_{bc}(h_b)}{\partial x_{i,b}} = \dots + m_a \frac{\partial W_{ab}(h_b)}{\partial x_{i,b}} + \dots \quad (27)$$

Comparing Eqs. (27), (26) and (25) we finally get:

$$\frac{\partial \rho_b}{\partial x_{i,a}} = \sum_{j=1}^d m_a c_{ij,b}(h_b) (x_{j,b} - x_{j,a}) W_{ab}(h_b). \quad (28)$$

Putting Eqs. (24) and (28) into Eq. (20) the i -component of the momentum equation for particle a reads:

$$\ddot{x}_{i,a} = - \sum_{b=1}^{n_b} m_b \left(\frac{P_a}{\Omega_a \rho_a^2} \mathcal{A}_{i,ab}(h_a) + \frac{P_b}{\Omega_b \rho_b^2} \mathcal{A}'_{i,ab}(h_b) \right), \quad (29)$$

being,

$$\mathcal{A}_{i,ab}(h_a) = \sum_{j=1}^d c_{ij,a}(h_a) (x_{j,b} - x_{j,a}) W_{ab}(h_a), \quad (30)$$

$$\mathcal{A}'_{i,ab}(h_b) = \sum_{j=1}^d c_{ij,b}(h_b) (x_{j,b} - x_{j,a}) W_{ab}(h_b). \quad (31)$$

Now it is straightforward to write a suitable energy equation as:

$$\left(\frac{du}{dt} \right)_a = \frac{P_a}{\Omega_a \rho_a^2} \sum_{b=1}^{n_b} \sum_{i=1}^d m_b (v_{i,a} - v_{i,b}) \mathcal{A}_{i,ab}(h_a). \quad (32)$$

Because magnitudes $\mathcal{A}_{i,ab}$, defined by Eqs. (30) and (31), are antisymmetric, the conservation properties of the IAD_0 formulation are identical as those of standard SPH.

As in standard SPH, an artificial viscosity term has to be added to stabilize the numerical scheme and to handle with shocks. The AV increases the effective pressure in those zones of the fluid which undergo compression. Including the viscous acceleration the momentum equation reads:

$$\ddot{x}_{i,a} = - \sum_{b=1}^{n_b} m_b \left(\frac{P_a}{\Omega_a \rho_a^2} \mathcal{A}_{i,ab}(h_a) + \frac{P_b}{\Omega_b \rho_b^2} \mathcal{A}'_{i,ab}(h_b) + \Pi_{ab} \tilde{\mathcal{A}}_{i,ab} \right), \quad (33)$$

where Π_{ab} accounts for the viscous pressure:

$$\Pi_{ab} = \begin{cases} \frac{-\alpha c_{ab} \mu_{ab} + \beta \mu_{ab}^2}{\bar{\rho}_{ab}} & \text{for } \mathbf{r}_{ab} \cdot \mathbf{v}_{ab} < 0, \\ 0 & \text{otherwise,} \end{cases} \quad (34)$$

where symbols have their usual meaning and \mathbf{r}_{ab} means $\mathbf{r}_a - \mathbf{r}_b$. The coefficient μ_{ab} is:

$$\mu_{ab} = \frac{\bar{h}_{ab} \mathbf{r}_{ab} \cdot \mathbf{v}_{ab}}{r_{ab}^2 + 0.01 \bar{h}_{ab}^2}. \quad (35)$$

To preserve momentum conservation the arithmetic mean of \mathcal{A} is taken:

$$\tilde{\mathcal{A}}_{i,ab} = \frac{1}{2} [\mathcal{A}_{i,ab}(h_a) + \mathcal{A}'_{i,ab}(h_b)]. \quad (36)$$

The inclusion of artificial viscosity in the energy equation leads to:

$$\left(\frac{du}{dt} \right)_a = \sum_{b=1}^{n_b} \sum_{i=1}^d m_b (v_{i,a} - v_{i,b}) \left(\frac{P_a}{\Omega_a \rho_a^2} \mathcal{A}_{i,ab}(h_a) + \frac{\Pi_{ab}}{2} \tilde{\mathcal{A}}_{i,ab} \right). \quad (37)$$

As a didactic example of the ability of the new scheme to handle subsonic physics let us consider the stability of an inhomogeneous system in mechanical equilibrium. A sample of $N=62\,500$ particles were evenly distributed in a square lattice with periodic boundary conditions so that initial density was set to $\rho_0 = 1 \text{ g.cm}^{-3}$. The density was then perturbed at random allowing maximum percent variations of 5% across the lattice. The internal energy of each particle was adjusted to ensure isobaricity with $P_0 = 1 \text{ dyn.cm}^{-2}$ leading to a sound speed value $c_s \approx 1.3 \text{ cm.s}^{-1}$. The evolution of the system was followed during almost a sound crossing time, $t_s \approx 0.5 \text{ s}$ using the three schemes: IAD , IAD_0 and standard SPH, with $n_b = 30$ and 100. Calculations using full IAD were carried out using the Eqs. (52) and (53) described in Sect. 5. From this on the word *standard*, STD, refers to the modern, fully conservative, Lagrangian formulation of SPH which explicitly includes the gradient of the smoothing length parameter in the scheme (see for instance Rosswog (2009) and references therein). The results of the simulations are summarized in Fig. 3, where it is shown the evolution of the standard deviation of pressure $P(t)$ with respect to P_0 for the three above mentioned schemes. It is clear that for this particular test both tensor schemes provide a better mechanical equilibrium than standard SPH during a sound crossing time, especially when full IAD is used. As expected the standard deviation of pressure decreases as the number of neighbors rises.

3.1. Computational issues

We are now more aware of the increase of computational burden of the integral method. With respect to memory requirements the nine coefficients (in 3D) of matrix \mathcal{T} and those belonging to matrix C can share the same memory space. Thus nine coefficients per particle have to be stored to compute $\mathcal{A}_{i,ab}$ in Eq. (33). While the increase in memory requirements are not especially bad the burden in speediness is larger. First of all one has to compute six of the nine coefficients of symmetric matrix \mathcal{T} , Eq. (22). Although these calculations involve simple operations they have to be done in a separate tree-walk because a previous knowledge of density is necessary. Afterwards matrix \mathcal{T} has to be inverted in order to calculate the coefficients $c_{ij,a}$ for particle a . Fortunately these matrix inversions do not take much time because they can be done out of the tree structure. Finally one has

to compute the nine quantities of coefficients $\mathcal{A}_{i,ab}$ associated to each pair of neighbors particles a, b ; instead of the three that are necessary in the standard formulation, and use them to compute both the momentum and the energy equations.

It is obvious that the proposed method demands a larger computational effort with respect to the standard SPH. Nevertheless, the extra burden could be low if the physical problem under simulation requires the calculation of long range forces (i.e. gravity) or involve complex physics (i.e. chemical or nuclear reactions, transport phenomena). Also note that, according to Figs. 1 and 2, if standard SPH had to achieve a similar accuracy as IAD_0 in calculating the first derivative the number of neighbors should be increased. To keep resolution the total number of particles had also to be increased in the same factor. Therefore changing both the number of neighbors and total number of particles could have a larger impact in the computational performance than using IAD_0 .

4. Hydrodynamic tests

The aim of this section is to check the theory described in the two precedent sections using four tests, all of them widely used in CFD. The two first simulations concern the growth of KH and RT hydrodynamic instabilities, where evolution always remains subsonic and, as we will see, the fully conservative IAD_0 scheme leads to improved results with respect to the standard method for the same identical initial conditions. The last two tests are related to strong supersonic flows where shock waves take over, as in the wall heating shock and Sedov tests, where again the use of the tensor route to estimate derivatives led to better results, especially for the wall heating shock test.

The simulations described in this section were carried out in Cartesian two dimensions because of the better achieved resolution, easiest initial setting and analysis of the results. Periodic boundary conditions were imposed in all tests except in the RT case, where fixed particles were taken on top and bottom of the box. A perfect gas Equation of State (EOS) $P = (\gamma - 1)\rho u$, being u the specific internal energy, with $\gamma = 5/3$ was always used. Coefficients α, β of artificial viscosity, in Eq. (34), were set to 1 and 2 respectively, except for the wall heating test where we took $\alpha = 1.5$, $\beta = 3$. The cubic spline was used to make the SPH interpolations but several calculations carried out with other interpolators (i.e. harmonic kernels with index $n=3$; Cabezón et al. (2008)) did not give significant differences. We use a self adaptive smoothing length parameter which keeps constant the number of neighbors of a given particle, n_b . Although the simulations described below were obtained using $n_b = 100$ the same calculations carried out using $n_b = 36$ neighbors did not give significant differences. Corrections due to the gradient of the smoothing length were explicitly included in the IAD_0 formulation as it comes from the Lagrange-Euler variational principle.

In Table 1 there is shown a summary of energy and momentum conservation properties of the different calculated models. The tensor calculations always give a better momentum and energy conservation than the standard ones for the same elapsed time. The bad energy conservation during the point-like Sedov explosion in all methods is due to the hard initial conditions. On the opposite side the very good conservation of momentum in the supersonic numerical experiments is partially due to the spherical symmetry imposed to the initial configurations.

4.1. Kelvin-Helmholtz instability

The Kelvin-Helmholtz instability is a well-known test to check the ability of any hydrodynamic code to handle subsonic perturbations. This instability appears when there is a sufficient velocity shear in the interface layer between two fluids with different densities. Small perturbations of the velocity field in the orthogonal direction to the interface grow up leading to a mixing of both fluids. This is usually simulated in a box with periodic boundary conditions where two fluid regions are defined with densities ρ_1 and ρ_2 respectively. Both layers have opposite parallel velocities leading to a shear discontinuity in the contact interface. In order to develop the instability a small perturbation is seeded in the interface as a sinusoidal mode of length scale λ .

In our case we have simulated a central band of high density fluid (ρ_1) moving in a low-density medium (ρ_2) in a squared lattice of 1 cm side in the XY plane using $N=62\,500$ particles. The mass of the particles was arranged in order to obtain the correct density profile following a ramp function Robertson et al. (2010). In this way we smoothed the interface density jump to make it comparable to the SPH resolution using

$$f(y) = \frac{1}{A} \frac{1}{1 + \exp\left(\frac{2(y-0.25)}{\Delta y}\right)} \frac{1}{1 + \exp\left(\frac{2(0.75-y)}{\Delta y}\right)}, \quad (38)$$

where A is a normalization constant and $\Delta y = 0.05$ cm. Therefore, the density profile was given by

$$\rho(y) = \rho_2 + (\rho_1 - \rho_2) f(y), \quad (39)$$

where $\rho_1 = 2 \text{ g.cm}^{-3}$ and $\rho_2 = 1 \text{ g.cm}^{-3}$.

The seed of the perturbation is obtained using a sinusoidal function for the v_y component of the velocity field. Then for the initial velocity we have

$$v_x(y) = v_2 + (v_1 - v_2) f(y), \quad v_y(x) = \Delta v_y \sin(n\pi x), \quad (40)$$

where we took $n = 2$ and $\Delta v_y = 0.1 \text{ cm.s}^{-1}$. Also note that the v_x component has been smoothed using the same ramp function used for the density. $v_1 = 0.5 \text{ cm.s}^{-1}$ and $v_2 = -0.5 \text{ cm.s}^{-1}$, which corresponds to the high and low density bands respectively.

Figure 4 shows four snapshots of the growth of the Kelvin-Helmholtz instability at different times for the calculation using IAD_0 (first row) and the standard SPH implementation (second row). As it can be seen the standard formulation does a poor job of resolving the structure of the instability. Although in the beginning the main shape is in gross agreement with the tensor simulations, the final image is blurry, the interface is not well defined and the shape is not correct. In the case of the tensor calculation the instability grows cleanly and at good rate, and the definition of the extremes of the billows, where the finest structure appears, is clearly enhanced. In order to achieve similar results to those obtained with the IAD_0 technique, different methods have been proposed to maintain the standard description, mainly based on including an artificial thermal conductivity (Price 2008). This method obtains good results, but includes a new set of parameters and estimates, like the maximum signal velocity between two particles to obtain a diffusion parameter. Even more, the inclusion of an artificial thermal conductivity leads to an extra dissipation of gradients away from discontinuities, therefore there is a need of a design of clever switches that control the amount of dissipation.

In Fig. 5 there is shown the evolution of total linear momentum during the development of the instability. Although both

schemes give a very satisfactory momentum conservation we can see that conservation using the IAD_0 method is at least one order of magnitude better than that of standard scheme.

In order to test the tensor approach in a more hostile scenario, we diminished the value of the amplitude of the initial velocity perturbation an order of magnitude (i.e. $\Delta v_y = 0.01 \text{ cm.s}^{-1}$). In third and fourth rows of Fig. 4 there are shown the results of the simulations using the configurations IAD_0 and STD . It is clear that in the standard formulation the instability *was unable* to grow, while it does using IAD_0 . Changing the geometry of the initial particle distribution from square to an uniform hexagonal lattice or reducing the size of the smoothing length taking $n_b = 36$ neighbors did not appreciably change the results. We can state then, that the matrix approach has inherent virtues that are absent in the standard formulation, mainly related with the generalization of the derivation technique to a tensor expression, which, in some sense, diminishes the errors derived from the discretization.

It is also worth to mention that during the simulations carried out using the standard calculation a generalized clumping of particles in the low density regions often appeared. This is a well-known problem, called pairing or tensile-instability, where particles get “stuck” if $r_{ij} < \frac{2}{3} h$ due to an unstable stress-strain relation that occurs typically when the second derivative of the kernel becomes negative and high strain is developed between particles. This problem eventually leads to difficulties in resolving distances between neighbors, incorrect interpolations and finally large non-physical behavior of the particles that halts the calculation. A typical way to cope with this problem is to adaptively change the kernel slope so that it becomes more centrally peaked (Cabezón et al. 2008). On the other hand, the IAD_0 method did not show this problem, hence we found that the tensor method seems to be less susceptible to pairing instability. The better behavior of matrix methods to cope with pairing instability has already been reported by other authors (Oger et al. 2007) deserving further investigation in the context of IAD_0 .

4.2. Rayleigh-Taylor instability

The simulation of the growth of the Rayleigh-Taylor instability in a stratified fluid in presence of gravity is a classical test of subsonic fluid dynamics. In its simplest form a box containing two fluids with different densities separated by a sharp transition region is put inside a gravitational field (Youngs 1984). If the denser fluid is located on top of the lighter the system becomes physically unstable and any small perturbation of the interface leads to fluid overturn. The denser fluid goes down and the lighter moves up giving rise to characteristic structures known as spikes and bubbles respectively. After a linear phase of growth, which can be studied analytically, the system enters in a complex non linear regime. In real fluids, however, the viscosity of the fluid prevents the growth of the instability for short wavelengths, thus viscosity tends to damp or even to completely suppress the instability. One serious problem of numerical schemes which incorporates the artificial viscosity formulation is that they introduce too much viscosity in the system, compromising the growth of instabilities. As we will see the integral approach to the derivative, Eqs. (33) and (37), leads to a substantial improvement in the simulation of the RT phenomenon when the initial perturbation amplitude is small.

A sample of $N=62\,500$ particles was distributed in a squared lattice of 1 cm side. The mass of the particles was conveniently arranged to reproduce the density profile given by:

$$\rho(x, y) = \begin{cases} \rho_2 & y \geq \Delta y \\ \left(\frac{\rho_2 - \rho_1}{2\Delta y}\right)y + \left(\frac{\rho_1 + \rho_2}{2}\right) & -\Delta y < y < \Delta y \\ \rho_1 & y \leq -\Delta y \end{cases} \quad (41)$$

where y is the vertical coordinate with the origin at the interface and Δy is the width of the transition zone between both fluids. The density in the two zones were set to $\rho_1 = 1 \text{ g cm}^{-3}$ and $\rho_2 = 2 \text{ g cm}^{-3}$ respectively, and the size of the transition zone was taken to $\Delta y = 0.05 \text{ cm}$.

The integration of the hydrostatic equilibrium equation gives the pressure distribution along the fluid:

$$P(x, y) = \begin{cases} -g \rho_2 \left(y - \frac{1}{2}\right); & y \geq \Delta y \\ -g \left[\rho_2 \left(y - \frac{1}{2}\right) + \left(\frac{\rho_2 - \rho_1}{4\Delta y}\right)(y^2 - \Delta y^2) + \left(\frac{\rho_1 + \rho_2}{2}\right)(y - \Delta y) \right]; & -\Delta y < y < \Delta y \\ g \left(\frac{\rho_2}{2} - \rho_1 y\right); & y \leq -\Delta y \end{cases} \quad (42)$$

where g is the gravity, here of value $g=0.5 \text{ cm s}^{-2}$. With this setting the speed of sound at the inter-phase is $c_s = 0.7 \text{ cm s}^{-1}$. A perturbation in the boundary layer with $\lambda = 0.25 \text{ cm}$ was seeded by giving an initial small vertical velocity v_y to the particles according to the following prescription (Abel 2011):

$$v_y(x, y) = \frac{\Delta v_y}{4} \left\{ 1 + \cos \left[8\pi \left(x + \frac{1}{4} \right) \right] \right\} \left\{ 1 + \cos \left[5\pi \left(y - \frac{1}{2} \right) \right] \right\}, \quad (43)$$

and v_y is set to zero for y positions above 0.7 cm and below 0.3 cm . The value of velocity perturbation was set to $\Delta v_y = 0.01 \text{ cm s}^{-1}$. In Fig. 6 there are shown several snapshots of the development of the Rayleigh Taylor instability calculated using IAD_0 . As we can see the RT instability is able to grow after a few tenths of second. When the same calculation was attempted using the standard SPH scheme to compute the acceleration the results were much worse, the instability was totally damped and there was no development of the RT fingers. As in the case of the Kelvin-Helmholtz instability changing the initial particle setting from the square to an hexagonal regular lattice or reducing the size of the smoothing length did not qualitatively alter the above conclusions. A similar conclusion was recently reported by (Abel 2011) who used a variant of standard SPH, albeit not fully conservative, to simulate the grow of the RT instability using a similar initial setting of the experiment. This negative result does not mean that standard SPH is not able to simulate this phenomena because it could handle it after a careful initial setting which minimizes the numerical noise. Nevertheless, the result of our simulations indicates that the tensor method is less dependent on the particular geometry of the initial lattice.

In Fig. 7 there is shown the evolution of the centre of mass of the spikes sample y_s from the initial contact surface. According to the theory the evolution is exponential during the initial stage $\xi(t) = \xi_0 \exp[\Gamma(t - t_0)]$, roughly until the initial perturbation ξ_0 at t_0 (here we took $t_0 = 1.1 \text{ s}$) has growth to a size $\xi_l \approx 1/k$ being k the wave number. In our tests $\xi_l \approx 0.04 \text{ cm}$. The theoretical growth rate Γ_t during the exponential phase is given by $\Gamma_t = \sqrt{A_t} k g$, where $A_t = (\rho_2 - \rho_1)/(\rho_2 + \rho_1)$ is the Atwood number. The exponential phase is followed by a brief second stage in

which the penetration of the dense fluid evolves as $y_s \propto gt^2$ until drag takes over and both falling spikes and rising bubbles reach a limiting speed. According to Fig. 7 all these features are present in the simulations. Nevertheless, there was only a qualitative agreement with the analytical growth rate during the initial exponential phase because the value of Γ inferred from the simulations was almost a half of the theoretical value. This is not surprising because a reliable quantitative estimation during the initial stage needs both a larger resolution as well as a better initial setting than that we are currently using. In particular the transition zone between light and dense fluids has to be sharper to correctly represent the Atwood number in this stage. An analytical expression for the terminal velocity of a rising bubble in a tube was obtained by Layzer (1955), $v_b = 0.51 \sqrt{A_t g l}$ where l is the radius of the tube. Taking $l = \lambda = 0.25 \text{ cm}$ we get $v_b = 0.104 \text{ cm.s}^{-1}$ in good agreement to the numerical value deduced from Fig. 7.

4.3. The wall heating shock test

We turn now to simulations concerning supersonic events. In the test known as the wall shock problem a spherical or cylindrical supersonic stream of gas is launched towards its geometrical centre forming a high compressed region. For these geometries, simulations can be compared to the predictions of an analytical approach to the evolution of thermodynamic variables as a function of the initial conditions (Noh 1987). Although the gross features of the event are correctly captured by SPH simulations it is well known that schemes which rely in artificial viscosity have difficulties to give a detailed description of the wall heating shock test. The reason is that AV spreads the shock over several computational cells, which induces an non-physical rise of internal energy ahead the shock. For converging flows a large artificial spike in internal energy is observed at the convergence centre. As a consequence a profound dip in the density profile appears to try to keep the pressure smooth. On the other hand the inclusion of a good amount of artificial viscosity is mandatory to handle the shock.

Our purpose behind this test was to discern if the integral route to calculate derivatives can lead to better results than the standard procedure. Therefore we use IAD_0 and use Eqs. (15), (33), (37) to carry out the simulations.

A sample of $N=57\,600$ particles with the same mass were evenly spread in a lattice so that the density was homogeneous, $\rho = 1 \text{ g cm}^{-3}$. The initial pressure and internal energy of particles were negligible. The system was obliged to implode by imposing a spherically symmetric velocity field $v_r = -1 \text{ cm s}^{-1}$. In Fig. 8 there are shown the density and radial velocity profiles at $t=0.3 \text{ s}$, when the shock is well developed. Basically both profiles follow a simple pattern which remains close to the analytical estimations. In the central region, $r < 0.1 \text{ cm}$ a plateau of compressed material forms, with a characteristic density of $\rho_s \approx 14.5 \text{ g cm}^{-3}$ a little lower than the analytical value, $\rho = 16 \text{ g cm}^{-3}$ for $\gamma = 5/3$ (Noh 1987). In this inner region matter remains stagnated with a velocity close to zero. Out of the plateau the density abruptly declines through the shock front trying to regain its initial value whereas the velocity goes up to reach $v_r = -1 \text{ cm s}^{-1}$ at the incoming, but still unshocked, matter. As we can see in Fig. 8 the simulation using the tensor approach is of better quality than that of standard derivatives. In particular the numerical oscillations in the post-shock region in both, density and velocity, were considerably reduced in the tensor formulation. Nevertheless the dip in

the density profile and the maximum value achieved by density were similar in both calculations.

4.4. Sedov test

In the Sedov test the evolution of a shock wave front born as a consequence of a point-like explosion is studied as it propagates in a homogeneous medium. The problem of an intense explosion in a gas is a standard test for hydrocodes being of relevance in astrophysics, where is not rare to find strong shocks in many scenarios involving fluid motions at high velocity. The theoretical solution was found by L.I. Sedov applying self-similar methods and dimensional analysis for different geometries (Sedov 1959). In its simplest formulation the Sedov problem has an initially cold gas at rest. At $t = 0$ s there is a point explosion at the origin which in Sedov (1959) was treated as an instantaneous release of energy at the origin and assumed that the background material through which the expanding gas sweeps behaves as a perfect gas. For these initial conditions there are precise, albeit algebraically complicated, analytical expressions for the fluid variables. In the case of SPH the artificial viscosity smears the shock over 2-3 times the smoothing-length. As a consequence the density jump across the shock front is always lesser than the factor four predicted by the theory for $\gamma = 5/3$. In more than one dimension resolution issues are crucial not only to resolve the peak of the blast wave but also to reproduce the correct post-shock variables downstream and the structure of the rarefied tail close to the origin. We want to investigate to what extent the use of the integral approach to the derivative can improve the results of the SPH simulations.

The initial setting was similar to that of the wall heating test but this time the velocity was set to zero everywhere at $t=0$ s so that the initial configuration is in equilibrium. To create the explosion a large amount of internal energy was instantaneously released in a small region around the centre of the box. To smooth the initial discontinuity we took an initial pressure step that decays as a Gaussian function,

$$P(r) = P_2 + (P_1 - P_2) \exp\left[\frac{-r^2}{\sigma^2}\right] \quad (44)$$

where P_1 and P_2 are the pressures in zones left and right around the step and σ sets the width of the pressure decay. In the present simulations $P_1 = 10^4$ dyn cm⁻² and $P_2 = 1$ dyn cm⁻² and $\sigma^2 = 36$ cm² which smooths the internal energy step over about 5-6 times the smoothing length. In Fig. 9 there are depicted the density and velocity profiles once the self-similar state has been achieved. As we can see the profiles calculated using the tensor and standard approaches to gradients do not differ so much. The peak in the density profile is about 80% of what it is expected from a strong shock moving through a $\gamma = 5/3$ gas but the profile in the post-shock zone is smoother in the calculation using IAD_0 . The velocity profile is also similar but the tensor calculation showed less oscillations and a more ordered behavior in the post-shock tail. These results are in agreement to the main conclusions given in the previous test dealing to the wall heating shock, reinforcing the idea that for identical initial settings IAD_0 leads to better results than standard derivatives also for supersonic events.

5. Handling linear phenomena: momentum and energy equations using IAD

Having both, exact linear interpolation and perfect momentum and energy conservation using either full IAD or other similar schemes seems to be difficult. In this respect the best physical systems to try to conciliate both things are pure linear systems for which linear acoustic wave propagation is a representative example. A suitable alternative SPH formulation can be found starting from the differential acceleration equation:

$$\ddot{\mathbf{r}} = -\frac{1}{\rho} \nabla P = -\left[\nabla\left(\frac{P}{\rho}\right) + \frac{P}{\rho^2} \nabla \rho\right], \quad (45)$$

which, using Eq. (10), can be easily accommodated within the SPH formalism:

$$\ddot{\mathbf{r}}_a = -\sum_b m_b \left(\frac{P_a}{\rho_a^2} + \frac{P_b}{\rho_b^2}\right) \nabla \tilde{W}_{ab}. \quad (46)$$

This equation can be deduced independently using the variational principle and, provided the kernel is symmetrized $\tilde{W}_{ab} = 0.5(W_{ab}(h_a) + W_{ab}(h_b))$, it conserves linear and angular momentum exactly. If, instead Eq. (10) we use Eq. (8) to compute Eq. (45) the resulting equation is:

$$\begin{aligned} \ddot{\mathbf{r}}_a = & -\left[\nabla\left(\frac{P}{\rho}\right) + \frac{P}{\rho^2} \nabla \rho\right] = \\ & -\sum_b m_b \left(\frac{P_a}{\rho_a^2} + \frac{P_b}{\rho_b^2}\right) \nabla \tilde{W}_{ab} + 2 P_a \sum_b \frac{m_b}{\rho_a \rho_b} \nabla \tilde{W}_{ab}. \end{aligned} \quad (47)$$

This particular form of the acceleration equation has several interesting features: 1) In the continuum limit it reduces to the standard expression, Eq. (46), because the last term in the equation vanishes. 2) As shown in Sect. 3.2 an isobaric system with smooth density gradients remains in equilibrium with negligible acceleration for a long time (see Fig. 3).

On the other hand it is also evident that the inclusion of the last term in Eq. (47) breaks its symmetry. Still, in the linear limit, momentum is conserved to a high extent as it can be easily demonstrated in 1D. Let us first expand the magnitudes P/ρ^2 in Eq. (47) assuming a smooth density gradient:

$$\frac{P_a}{\rho_a^2} \simeq \frac{P_a}{\rho_a \rho_b} \left(1 - \frac{\Delta \rho}{\rho_b}\right); \quad \frac{P_b}{\rho_b^2} \simeq \frac{P_b}{\rho_a \rho_b} \left(1 + \frac{\Delta \rho}{\rho_a}\right) \quad (48)$$

being $\Delta \rho = \rho_a - \rho_b$ and it was taken $|\Delta \rho|/\rho \ll 1$. Inserting the approach (48) into Eq. (47) and neglecting high order terms the acceleration reads:

$$\ddot{x}_a = -\frac{\sum_b \frac{m_b}{\rho_b} \left(\frac{P_b - P_a}{\rho_a}\right) (x_b - x_a) W_{ab}}{\sum_b \frac{m_b}{\rho_b} (x_b - x_a)^2 W_{ab}} \quad (49)$$

Which for a linear pressure profile within the kernel domain of the particle:

$$P_b = P_a + \left(\frac{\partial P}{\partial x}\right)_a (x_b - x_a), \quad (50)$$

becomes:

$$\ddot{x}_a = -\frac{1}{\rho_a} \left(\frac{\partial P}{\partial x}\right)_a, \quad (51)$$

which is just the one-dimensional Newton equation, thus leading to an exact value for the acceleration. In consequence global momentum is well preserved provided the system remains in the linear regime and density gradients are smooth. According to this discussion we complete the acceleration equation obtained in Sect. 3 using the IAD_0 scheme with a corrective term:

$$\ddot{x}_{i,a} = - \sum_{b=1}^{nb} m_b \left(\frac{P_a}{\Omega_a \rho_a^2} \mathcal{A}_{i,ab}(h_a) + \frac{P_b}{\Omega_b \rho_b^2} \mathcal{A}'_{i,ab}(h_b) + \right. \\ \left. \Pi_{ab} \tilde{\mathcal{A}}_{i,ab} - \frac{\Psi P_a}{\rho_a \rho_b} \mathcal{A}_{i,ab}(h_a) \right) \quad (52)$$

where $0 \leq \Psi \leq 2$ is a parameter controlling the strength of the applied correction. For $\Psi = 0$ the already checked IAD_0 scheme results, whereas for $\Psi = 2$ we have full linear IAD .

To take into account the corrective term in the energy equation we include the power released/absorbed by such term in Eq. (37):

$$\left(\frac{du}{dt} \right)_a = \sum_{b=1}^{nb} \sum_{i=1}^d m_b (v_{i,a} - v_{i,b}) \cdot \left(\frac{P_a}{\Omega_a \rho_a^2} \mathcal{A}_{i,ab}(h_a) + \right. \\ \left. \frac{\Pi_{ab}}{2} \tilde{\mathcal{A}}_{i,ab}(h_b) - \frac{\Psi P_a}{\rho_a \rho_b} v_{i,a} \mathcal{A}_{i,ab}(h_a) \right). \quad (53)$$

so that total energy is exactly conserved. In the case of very subsonic movements the energetic contribution of the correction term is small. For $\Psi = 0$ Eqs. (52) and (53) reduces to the fully conservative IAD_0 scheme. Alternatively, the case with $\Psi = 2$ could be used to handle linear systems with smooth density gradients as it shows enhanced interpolation abilities and good conservative properties.

Sound wave propagation is an example of a system which evolves in the linear limit of Euler equations. It is therefore a test ideally suited to highlight the potential advantages of the IAD scheme. An homogeneous system with $\rho_0 = 1 \text{ g cm}^{-3}$ was simulated using $N=62\,500$ particles uniformly distributed in a lattice of size 1 cm. The initial values of both pressure and density were set to one. A sample of $n_p = 200$ particles inside a circle of radius $R_p = 0.032 \text{ cm}$ located at the centre of mass of the lattice was obliged to oscillate with small amplitude and period P . Such compact sample of particles was mimicking the effect of an external oscillating *piston* moving adiabatically onto the initially unperturbed gas. As the *piston* moves it launches regular trains of circular waves which propagate at the sound speed $c_s = \sqrt{\gamma P / \rho} = 1.29 \text{ cm s}^{-1}$ for $\gamma = 5/3$. We want to check the ability of the different before mentioned schemes to handle with this problem.

Particles belonging to the *piston* move homologously, following the harmonic oscillator law:

$$v_r(r, t) = v_r^m(r) \cos(\omega t) \quad (54)$$

where ω stands for the angular frequency, and the maximum value of the radial velocity of a particle located at distance r from the center is:

$$v_r^m(r) = v_r^m(R_p) \left(\frac{r}{R_p} \right) \quad (55)$$

Resolution issues put limits in both the period and the maximum velocity at the *piston* head $v_r^m(R_p)$. The value of the period

was set to $P=0.05 \text{ s}$ so that around eight complete waves were launched before the first one is reaching the limits of the system. The value of the maximum velocity at the piston head was set to $v_r^m(R_p) = 0.16 \text{ cm s}^{-1}$.

The results of the simulations for the three SPH approaches: IAD , IAD_0 and Standard are summarized in Fig. 10 which represents the radial velocity profile of the gas at time $t=0.35 \text{ s}$. It is quite evident that the spherical symmetry was better preserved during the IAD calculation, while there is a progressive degradation of the symmetry in the IAD_0 and standard calculations respectively. The worst case corresponds to the standard scheme but even in this case spherical symmetry is reasonably preserved. A more quantitative analysis can be done making use of the analytical solution of diverging circular waves, usually known as a waves in a membrane in the literature. The solution for free harmonic traveling waves in a circular membrane is written as:

$$A(r, t) = A_m J(u) \cos(\omega t) \quad (56)$$

where $u = kr$, being k the wave number and $J(u)$ is the Bessel function with radial and angular modes $m=n=0$. Bessel functions are constrained by $J(0) = 1$ at the center of the wave train. The profile for the radial velocity given by expression (56) with $A_m = v_r^m(R_p)$ and the comparison with the numerical profiles obtained using the different schemes are also shown in Fig. 10. The analytical solution reminds one of a damped cosine wave propagating at the sound speed $c_s = 1.29 \text{ cm}^{-1}$. On the whole the three schemes were able to correctly track the evolution of the waves. However a close inspection reveals small differences among them. The best value in the wave velocity corresponds to the IAD_0 scheme, $c_s^{iad_0} = 1.285 \text{ cm}^{-1}$ followed by the standard $c_s^{std} = 1.267 \text{ cm}^{-1}$ whereas full IAD falls a bit short $c_s^{iad} = 1.25 \text{ cm}^{-1}$. Even though the damping in the three schemes is always larger than that of analytical solution it seems that the worst case also corresponds to the fully IAD scheme built setting $\Psi = 2$ in Eqs. (52) and (53).

The simulation of linearized systems represents the most favoured situation to apply exact linear interpolation schemes such as IAD because, as shown above, conservation of momentum and energy is probably as good as in the standard formulation. Nonetheless the numerical experiments with the acoustic waves suggested limited advantages of using these schemes. In fact some details of the wave evolution are better represented by IAD_0 or even by the standard scheme. Only the spherical symmetry was better preserved in the experiments using IAD .

6. Applying IAD_0 to astrophysics: the stability of a sun-like polytrope

Applying Eqs. (15), (33) and (37) to astrophysics is straightforward by just adding the gravitational acceleration to the momentum equation. We approached gravity using a multipolar expansion of the force (Hernquist & Katz 1989), up to quadrupole contributions. The three-dimensional structure of a sun-like polytrope was simulated using a sample of $N = 10^5$ particles with equal mass. To achieve the equilibrium we have proceeded in three stages. First, the radial coordinate of each particle was set following the one dimensional density profile of the polytrope with its angular position determined at random. In the second stage we allowed the particle sample to relax under the action of pressure and gravity forces but the movement of the particles was constrained to keep constant their distance to the centre. In a third stage we let the particle sample free to approach the

equilibrium configuration. We have followed the third stage using both IAD_0 and STD schemes with the AV coefficients set to $\alpha = 1, \beta = 2$. The main goal of this test is to show that IAD_0 (and probably other matrix methods) can be used to simulate astrophysical scenarios with good results, excellent conservation properties and with low computational penalty.

In Fig. 11 (upper row) there is depicted the evolution of density for two particles initially located at the centre and at the surface of the star respectively. As we can see these particles display the typical oscillatory behavior in both regions. As expected the amplitude of the oscillations is small close to the centre and larger at the surface. The relaxation towards equilibrium is slower for the tensor method but the structure of the star after $t = 2$ h of relaxation is very similar. It was checked that, with the exception of a tiny region close to the surface, the gradient of pressure matched gravity along the polytrope in both calculations. In Fig. 11 (lower row) we show the evolution of the kinetic energy and the instantaneous position of the centre of mass during the relaxation process. The evolution is similar in both calculations but the level of kinetic energy always remained a bit higher when IAD_0 is used. The energy conservation after two hours of evolution was rather good for both schemes $\approx 3 \cdot 10^{-5}$. In the bottom right of Fig. 11 there is shown the evolution of the moduli of the centre of mass position. We see that momentum is not perfectly conserved during the simulation in both simulations, mainly due to the multipolar approach to the gravitational force. Still the tensor scheme provides a better conservation of momentum than the standard SPH calculation.

The higher level of kinetic energy and the slower relaxation rate towards complete mechanical equilibrium shown by IAD_0 suggest that for disordered systems the numerical noise could be higher for the tensor method. As shown in Fig. 11 the recalculation of the evolution of the polytrope using larger values for the AV coefficients, $\alpha = 1.5, \beta = 3$ led to a significant reduction of the level of spurious kinetic energy while the evolution of the density at the center and surface of the star remained unaltered. This points to the numerical noise as the main agent responsible for the excess of kinetic energy seen during the relaxation process.

To explore the performance of the algorithm the tolerance parameter, θ , controlling the accuracy of the multipolar expansion was varied from $0 \leq \theta \leq 1$, where $\theta = 0$ corresponds to direct particle to particle interaction. Such benchmarking analysis is summarized in Fig. 12. We see that for standard values of the tolerance parameter, $\theta \approx 0.7$, widely used in current SPH calculations the computational overload is around 40%. Such overload rapidly decays as $\theta \rightarrow 0$, as expected. On the other hand the number of operations in the multipolar calculation of gravity scales as $\approx N \log N$ (Hernquist & Katz 1989). Therefore it is expected a reduction in the computational overload with increasing number of particles. Nevertheless, it is worthy to state here that all these calculations were performed using a serial code. A nice property of SPH is that only a single tree-walk is needed in order to find the neighbors (and calculate gravity if needed). Once this information is available the remaining calculations (density, momentum and energy equations, IAD_0 terms) can be performed with linked-lists which can be directly parallelized. Following that idea we found that for a $2 \cdot 10^5$ particles 3D simulation in a standard 4-core desktop computer the gravity calculation (which remains serial) takes around 30 times more wall-clock time than the rest of the calculations together (parallelized with OMP using 4 cores). Knowing this, the computational overload due to the IAD_0 calculation remains sub-dominant.

7. Conclusions

A novel procedure (IAD) to evaluate gradients in the context of SPH has been described and checked along the previous pages. The mechanism to make derivatives relies in an integral approach which ensures that the derivative of a linear function is exactly obtained, even after transforming integrals to summations. The price to pay is an increase in the algebraic complexity because gradients are estimated using the tensor expression given by Eq. (4). Still, the new scheme is not much more complex than the standard one, being easy to implement and it includes the classical formulation as a particular case. A shortcoming of the method is that it leads to non-conservative movement equations. Thus we have developed and checked a restricted interpretation of the method, referred as IAD_0 along the manuscript, which sacrifices exact linear interpolation in order to have perfect conservation of momentum and energy. Analytical considerations and numerical experiments described in Sects. 2 and 4 strongly suggest that IAD_0 behaves better than the standard method to compute gradients. The modified momentum equation obeying these derivative rules was developed in Sect. 3, resulting in Eq. (29). As the movement equation was obtained from the Euler-Lagrange variational principle assuming isentropic evolution the ensuing equation was fully conservative and explicitly included the ∇h terms. A conservative energy equation compatible with the momentum equation was also developed. To handle with shocks the scheme was completed with the inclusion of the standard artificial viscosity formalism resulting in Eqs. (33) and (37), which along the density equation, expression (15), summarizes the mathematical formalism linked to IAD_0 .

The formulation of SPH using matrix methods based on the variational approach (Bonet & Lok 1999) has been used in CFD to successfully simulate a variety of problems (generally in two dimensions) from fluids to impact and fracture of solid bodies. Nevertheless, none of these schemes are able to simultaneously achieve re-normalization, exact momentum and energy conservation, perfect linear interpolation and to implicitly include the gradient of the smoothing length in the equations (Oger et al. 2007). Neither IAD_0 can do but probably is the more optimal formulation because it fulfills almost all the above requirements with a moderate computational overload.

Four tests were run in two dimensions in order to check the performance of the method (see Table 1), two of them in connection to bi-dimensional subsonic hydrodynamic evolution (KH and RT instabilities) and the other two related to the description of highly supersonic phenomena such as the wall heating shock and the Sedov tests. In all cases the performance of the new scheme was superior, although in the supersonic numerical experiments the improvement was modest. The tests concerning the growth of the Kelvin-Helmholtz and Rayleigh-Taylor instabilities clearly showed the power of the IAD_0 scheme because no growth at all was seen when the standard scheme was used with small initial perturbations, whereas instabilities were able to grow when IAD_0 was used. Of course this does not mean that standard SPH technique can not give a satisfactory answer for these problems but simply states that for the same initial conditions the tensor method seems to be more stable and sensible to small perturbations. Therefore these results point out that simulations using the IAD_0 scheme are less dependent on the initial setting of the particles. As expected from a tensor method such feature could probably be reinforced as dimensionality increases.

In Sect. 5 we have devised and discussed a slightly different formulation which combines exact linear interpolation and good

conservative properties, Eqs. (52) and (53). The main point here is that the fully IAD method would be only useful to handle linearized systems with smooth density gradients. Nevertheless a single parameter allows to easily switch from IAD to IAD_0 and in this sense the formulation given in Sect. 5 is more general. As sound waves are the prototype of a linearized system we have used the new scheme to simulate the two dimensional propagation of acoustic waves. The simulations indicate that there are no especial advantages of using IAD instead IAD_0 or standard SPH, because only the symmetry was better preserved during the evolution of the wave trains.

A preliminary application of IAD_0 to astrophysics was discussed in Sect. 6 in connection to the stability of a sun-like star described by a polytropic EOS. The main goal was to demonstrate that matrix SPH methods can be used to handle three dimensional self gravitating bodies with satisfactory results and to explore the real computational overload when long range forces need to be computed. For a reasonable accuracy in the calculation of gravity we have estimated a computational overload $< 50\%$ for a serial code, with respect to that of standard SPH, when a multipolar expansion is used to calculate the gravitational force. The overload becomes negligible for an exact particle to particle calculation of gravity scaling as $N^2/2$.

To summarize we could say that simulations carried out using the SPH scheme obtained with the IAD_0 approach to the gradients always led to improved results with respect to standard SPH. As the new scheme is both fully conservative and more precise making interpolations it could be an alternative to the standard technique to handle systems subjected to small perturbations. Such idea is supported by the numerical study of the growth of Kelvin-Helmholtz and Rayleigh-Taylor instabilities. On the other hand simulations of supersonic phenomena were also improved when the tensor approach was used. The main drawback of the method is that it increases the computational overload, but one has to keep in mind that there is not always a linear relationship between algebraic complexity and computational charge. This could be the case of hydrocodes which incorporate time consuming physics or if the SPH algorithm built with IAD_0 allowed to a larger time steps. Even more, using linked-lists a direct parallelization of the method is possible as the calculations are carried out of the tree-walk, keeping the computational overload due to the IAD_0 almost negligible in front of more time consuming sections of the code.

Although the presented results are encouraging more work needs to be done to confirm and extend the conclusions of our proposal. For the most part the tests presented in this work to validate the scheme were carried out in two dimensional boxes using well ordered initial models. The simulation of realistic astrophysical scenarios generally involves, however, a quite different numerical setting. Many of these calculations have to be performed in three dimensions using a random-like initial particle distribution and incorporating the long range gravitational force. A detailed comparative analysis of the ability of IAD_0 and standard SPH to cope with these scenarios is beyond the scope of the present work and is left for a forthcoming publication. Nonetheless, we can advance a couple areas of difficulty regarding the tensor formulation which probably will come up in astrophysical 3D applications of the method: 1) As suggested in Sect. 6 the tensor method could be more sensible to the disorder of the particles and display a higher level of numerical noise than the standard scheme. 2) Free boundary conditions could be more difficult to handle using IAD_0 because the simplificative hypothesis assumed in Eq. (14) does not hold at the edge of the system. The difficulty to simulate sharp boundaries with matrix

methods is a well known problem of MLS schemes. According to Oger et al. (2007) it can be solved just by taking special conditions at the limits of the system. This is not, however, a big concern in astrophysics because astronomical bodies never end abruptly. Regarding this point the stability test of the sun-like star discussed in Sect. 6 does not reveal a bad behaviour of the particles located close to the surface. Although the initial unbalance between gravity and pressure gradient is more pronounced than in the standard formalism, the ensuing evolution towards equilibrium is not much different.

Acknowledgements

The authors acknowledge fruitful discussions with Antonio Relaño and Fayyaz Ahmad regarding the SPH technique. This work has been funded by the Spanish MEC grants AYA2010-15685, AYA2008-04211-C02-C01 and the Swiss Platform for High-Performance and High-Productivity Computing within the *supernova* project. It was also supported by DURSI of the Generalitat de Catalunya. The rendered SPH plots were made using the freely available *SPLASH* code (Price 2007).

References

- Abel T., 2011, MNRAS, 413, 271
- Brookshaw L., 1985, Proc. Astron. Soc. Aust., 6, 207
- Bonet, J., Lok, T.S.L, 1999, Computer Methods in Applied Mechanics and Engineering 180, 97
- Cabezón R.M., García-Senz D., Relaño A., 2008, J. Comput. Phys., 227, 8523
- Dilts G.A., 1999, Int. J. Numer. Methods, 44, 1115
- Gingold R.A., Monaghan J.J, 1977, MNRAS, 181, 375
- Hernquist, L., Katz, N., 1989, ApJS, 70, 419
- Layzer, D. 1955, ApJ, 122, 1
- Lucy L.B., 1977, AJ, 82, 1013
- Monaghan J.J, 1992, ARAA, 365, 199
- Monaghan J.J, 2005, Rep. Prog. Phys., 68, 1703
- Morris J., Monaghan J.J., 1997, J. Comput. Phys., 136, 41
- Noh W.F., 1987, J. Comput. Phys., 72, 78
- Oger, G., Doring, M., Alessandrini, B., Ferrant, P., 2007, J. Comput. Phys., 225, 1472-1492
- Price D., 2007, PASA, 24, 159
- Price D., 2008, J. Comput. Phys., 227, 10040.
- Robertson B.E., Kravtsov A.V., Gnedin N.Y., Abel T., Rudd D.H., 2010, MNRAS , 401, 2463
- Rosswog S., 2009, New Astronomy Review, 53, 78
- Sedov L.I., Similarity and Dimensional Methods in Mechanics. Academic Press Inc. 1959.
- Springel, V., Hernquist, L., 2002, MNRAS , 333, 649.
- Youngs D., 1984, Physica 12 D, 32

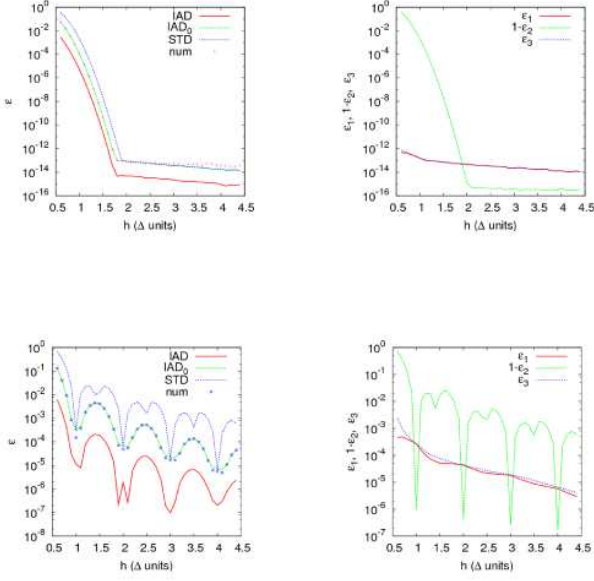


Fig. 1. Relative error ϵ in the first derivative of density $\rho(x) = (1+x) \text{ g cm}^{-3}$ as a function of the smoothing length (in interparticle units) calculated using both tensor and standard SPH schemes. Crosses are for direct $\frac{\rho_b - \rho_a}{x_b - x_a}$ derivative estimation. Upper left is for the error when the Gaussian kernel is used. The upper right picture shows the contribution of several error sources to the total error ϵ . Bottom pictures are the same but for the cubic-spline kernel.

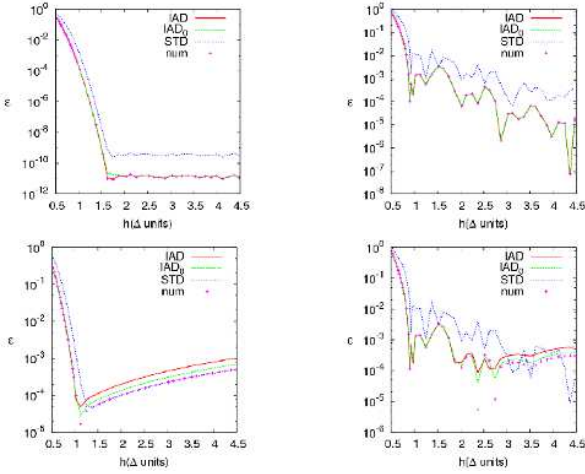


Fig. 2. Relative error ϵ in the first derivative of linear functions calculated in 2D as a function of the smoothing length. Upper rows depict the value of ϵ for $\rho(x,y) = (1+x) \text{ g cm}^{-3}$ obtained using the Gaussian (left) and the cubic spline (right) kernels. Bottom rows are the same but for the function $\rho(x,y) = 1 + \sqrt{x^2 + y^2} \text{ g cm}^{-3}$. Error profiles with crosses are for the direct $\frac{\rho_b - \rho_a}{r_b - r_a}$ derivative estimation.

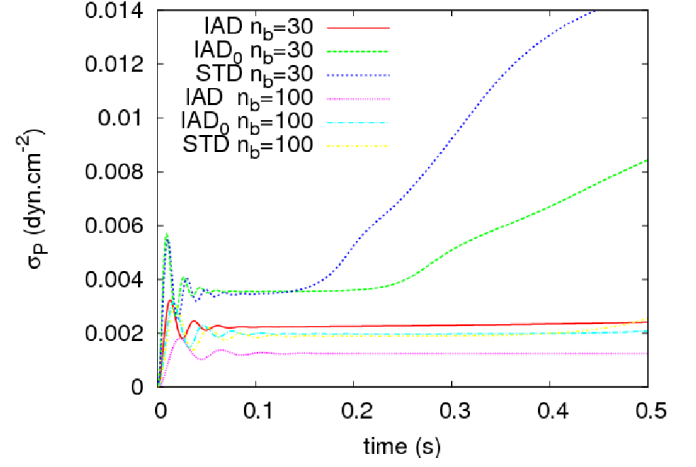


Fig. 3. Evolution of magnitude $\sigma_{P(t)} = \sqrt{\frac{\sum_b (P_b - P_0)^2}{N}}$ of an inhomogeneous 2D system, initially in hydrostatic equilibrium, calculated using the different SPH schemes mentioned in the text.

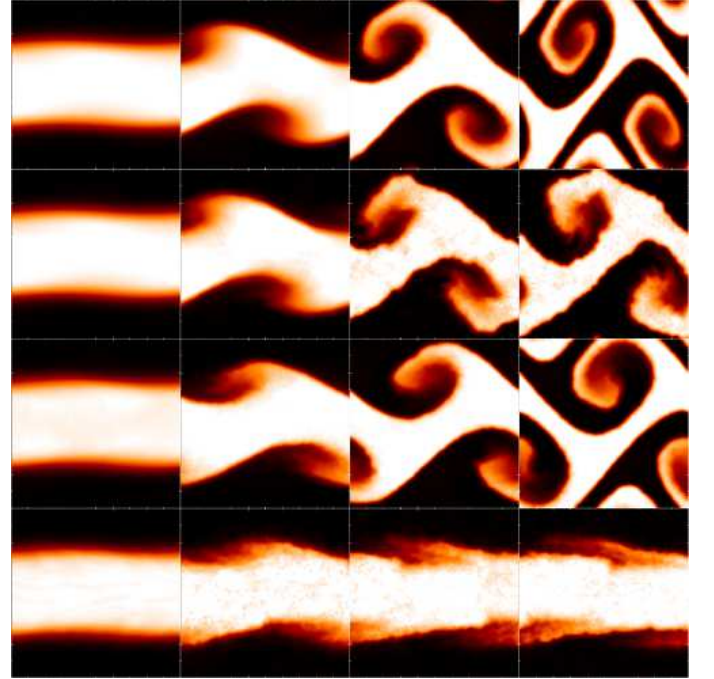


Fig. 4. Evolution of the Kelvin-Helmholtz instability. The snapshots show the color map of density at times $t = 0.1, 1.0, 2.0$ and 3.0 s for methods IAD_0 (first row) and standard SPH (second row), with $\Delta v_y = 0.1 \text{ cm s}^{-1}$. Times $t = 1.0, 3.0, 4.0$ and 5.0 s for methods IAD_0 (third row) and standard SPH (fourth row), with $\Delta v_y = 0.01 \text{ cm s}^{-1}$.

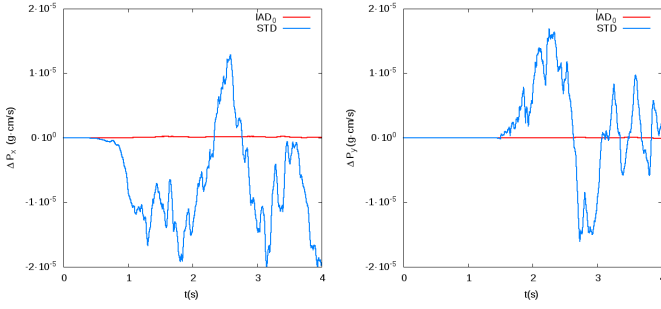


Fig. 5. Evolution of the absolute deviation from initial linear momentum during the development of the Kelvin-Helmholtz instability. Figure on the left is for the x component of total momentum calculated using IAD_0 and standard (STD) schemes whereas figure on the right is the same for the y component.



Fig. 6. Development of the Rayleigh-Taylor instability for Atwood number 1/3 calculated using the IAD_0 scheme. The snapshots show the color map of density at times $t = 0.4, 4.2, 5.1$ and 5.7 s.

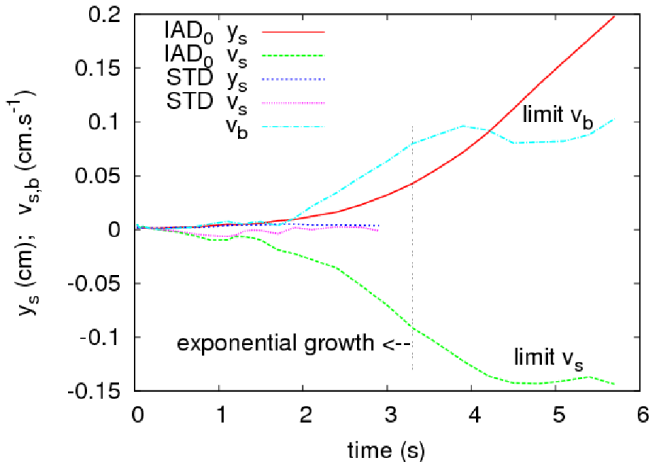


Fig. 7. Evolution of the center of mass of the spikes during the growth of the Rayleigh-Taylor instability depicted in Fig. 6. The velocity of the center of mass of the bubbles, v_b , and spikes, v_s , is also shown. For $t > 4$ s a limiting speed is reached.

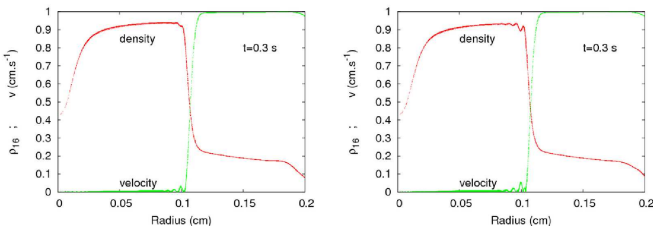


Fig. 8. Density and velocity profiles during the wall heating shock test. Figure on the left is for IAD_0 calculation whereas figure on the right is for the simulation using the standard SPH scheme. Density is normalized to 16 g cm^{-3} .

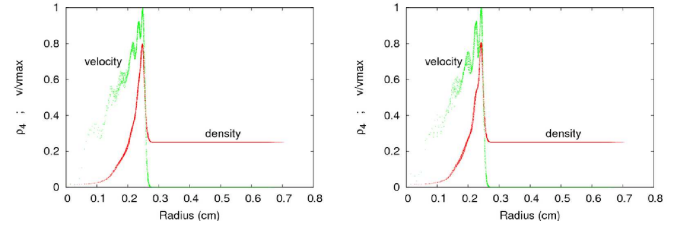


Fig. 9. Density and velocity profiles during the Sedov test. Figure on the left is for IAD_0 calculation whereas figure on the right is for the simulation using the standard SPH scheme. Density is normalized to 4 g cm^{-3} .

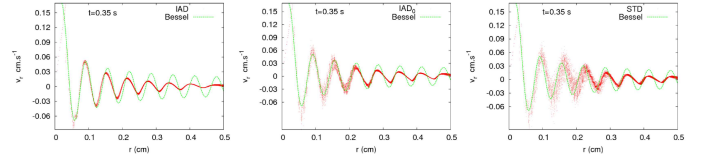


Fig. 10. Acoustic wave profiles at $t=0.35$ s calculated using IAD , IAD_0 and standard SPH (STD). The waves were generated by the periodic displacement of a circular piston of size 0.035 cm located at the center of the lattice. The continuum line is the analytical solution calculated taking sound speed $c_s = 1.29 \text{ cm s}^{-1}$.

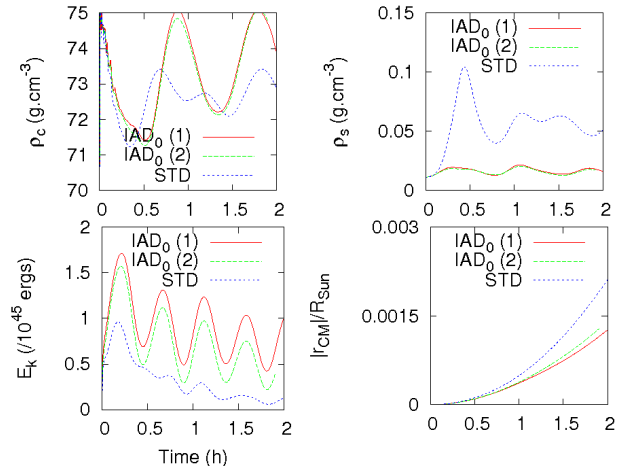


Fig. 11. Evolution towards stability of a sun like-star approached by a polytrope. Calculations were carried out using IAD_0 and the standard, STD, schemes. Labels $IAD_0 (1)$ and $IAD_0 (2)$ refer to calculations with the AV parameters set to $\alpha = 1, \beta = 2$ and $\alpha = 1.5, \beta = 3$ respectively.

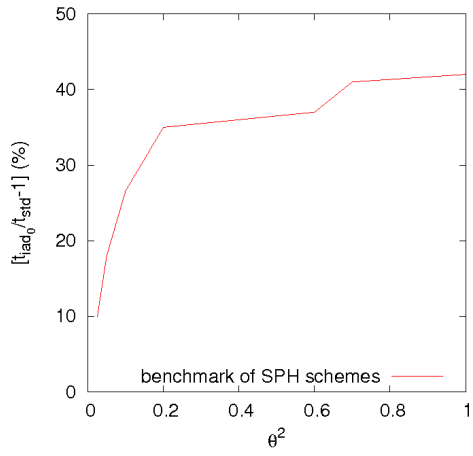


Fig. 12. Benchmarking of IAD_0 versus STD. Parameter θ is the tolerance parameter assumed in the multipolar calculation of gravity.

Test	Scheme	Time (s)	$ \Delta E /E_0$	$ \Delta x_{cm} /R$	$ \Delta y_{cm} /R$
KH	IAD_0	4.0	$4.0 \cdot 10^{-8}$	–	$3 \cdot 10^{-5}$
KH	STD	4.0	$1.0 \cdot 10^{-6}$	–	$1.3 \cdot 10^{-4}$
RT	IAD_0	5.7	$1.2 \cdot 10^{-5}$	$5 \cdot 10^{-5}$	–
RT	STD	5.7	no grow	no grow	–
WH	IAD_0	0.3	$5.9 \cdot 10^{-3}$	$8 \cdot 10^{-12}$	$8 \cdot 10^{-12}$
WH	STD	0.3	10^{-2}	$5 \cdot 10^{-10}$	$5 \cdot 10^{-10}$
SED	IAD_0	0.7	$9.8 \cdot 10^{-2}$	$1.3 \cdot 10^{-10}$	$1.3 \cdot 10^{-10}$
SED	STD	0.7	$1.4 \cdot 10^{-1}$	$1.5 \cdot 10^{-10}$	$1.6 \cdot 10^{-10}$

Table 1. Conservation properties of the computed models: Kelvin-Helmholtz (KH), Rayleigh-Taylor (RT), the wall heating shock (WH) and Sedov (SED). Conservation of momentum is tracked by normalizing the deviation of the center of mass by the characteristic size of the system R . See Fig. 5 for the temporal evolution of the momentum in the KH case. The method used to calculate the derivatives IAD_0 or standard, STD, is indicated.